Cell Reports
Medicine

Article

Near-infrared fluorescence imaging with an MET-targeting probe for biopsy site selection in patients with oral potentially malignant disorders

Graphical abstract

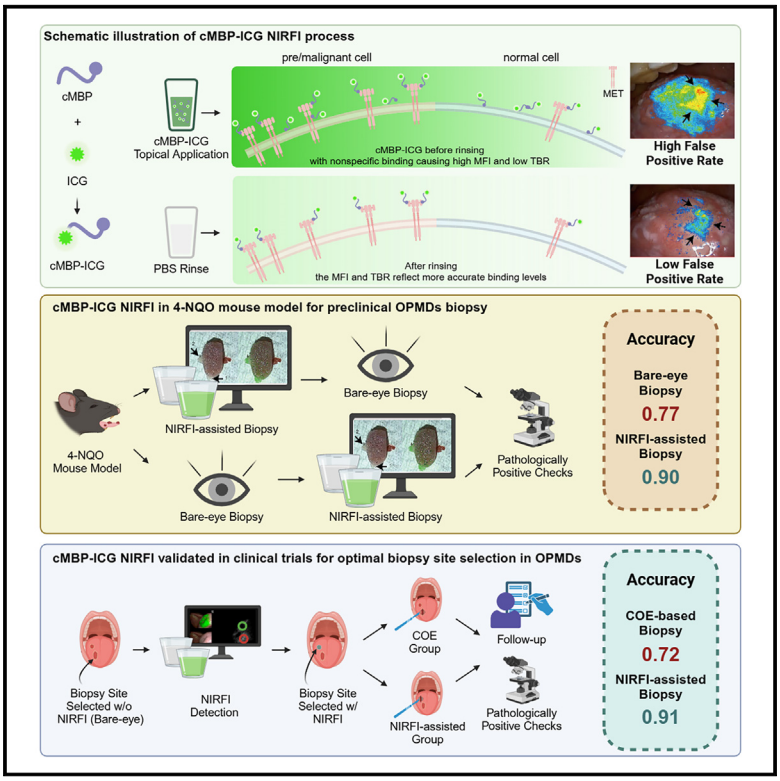

Highlights

- 4-NQO mouse model replicated OPMD progression to OSCC
- NIRFI improved detection accuracy of precancerous lesions by 23% in 4-NQO model
- NIRFI-assisted biopsy achieved 100% sensitivity and 86% specificity in clinical trial
- NIRFI-assisted biopsy outperformed COE in detecting HGD/SCC in patients with OPMDs

Authors

Jingbo Wang, Xuemin Shen, Qifan Ma, ..., Jie Tian, Ying Yuan, Xiaofeng Tao

Correspondence

tian@ieee.org (J.T.),
yuany83@163.com (Y.Y.),
cjr.taoxiaofeng@vip.163.com (X.T.)

In brief

Wang et al. evaluate the use of near-infrared fluorescence imaging (NIRFI)-assisted biopsy with cMBP-ICG to detect malignant transformation in oral potentially malignant disorders. In our preclinical model and clinical trial studies, NIRFI has demonstrated higher diagnostic accuracy than conventional methods, supporting its potential to improve early intervention and outcomes of OSCC.

Wang et al., 2025, Cell Reports Medicine 6, 101978
March 18, 2025
https://doi.org/10.1016/j.xcrm.2025.101978

CellPress

Cell Reports Medicine

CellPress
OPEN ACCESS

Article

Near-infrared fluorescence imaging with an MET-targeting probe for biopsy site selection in patients with oral potentially malignant disorders

Jingbo Wang,[1,12] Xuemin Shen,[2,3,12] Qifan Ma,[1,12] Lin Yang,[1,4,12] Xiaoyu Zhou,[5] Luting Wang,[5] Junqi Cui,[6] Chunye Zhang,[6] Guojun Li,[7] Neil Gross,[7] Siyi Li,[3,8] Ruimin Huang,[9] Changyou Zhan,[10] Zhen Cheng,[5] Kun Wang,[11] Jie Tian,[11,*] Ying Yuan,[1,*] and Xiaofeng Tao[1,13,*]

[1]Department of Radiology, Shanghai Ninth People's Hospital, Shanghai Jiao Tong University School of Medicine, Shanghai 200011, China
[2]Department of Oral Mucosal Diseases, Shanghai Ninth People's Hospital, College of Stomatology, Shanghai Jiao Tong University School of Medicine, Shanghai 200011, China
[3]National Clinical Research Center for Oral Diseases, Shanghai Key Laboratory of Stomatology & Shanghai Research Institute of Stomatology, Shanghai 200011, China
[4]Department of Radiology, Fujian Branch of Shanghai Children's Medical Center, Fujian Children's Hospital, Fujian 350014, China
[5]State Key Laboratory of Drug Research, Molecular Imaging Center, Shanghai Institute of Materia Medica, Chinese Academy of Sciences, Shanghai 201203, China
[6]Department of Pathology, Shanghai Ninth People's Hospital, Shanghai Jiao Tong University School of Medicine, Shanghai 200011, China
[7]Department of Head and Neck Surgery, The University of Texas MD Anderson Cancer Center, Houston, TX 77030, USA
[8]Department of Oral & Maxillofacial-Head & Neck Oncology, Shanghai Ninth People's Hospital, College of Stomatology, Shanghai Jiao Tong University School of Medicine, Shanghai 200011, China
[9]Center for Drug Safety Evaluation and Research, Shanghai Institute of Materia Medica, Chinese Academy of Sciences, Shanghai 201203, China
[10]Department of Pharmacology, School of Basic Medical Sciences & Center of Medical Research and Innovation, Shanghai Pudong Hospital & State Key Laboratory of Molecular Engineering of Polymers, Fudan University, Shanghai 200433, China
[11]CAS Key Laboratory of Molecular Imaging, Beijing Key Laboratory of Molecular Imaging, The State Key Laboratory of Management and Control for Complex Systems, Institute of Automation, Chinese Academy of Sciences, Beijing 100190, China
[12]These authors contributed equally
[13]Lead contact
*Correspondence: tian@ieee.org (J.T.), yuany83@163.com (Y.Y.), cjr.taoxiaofeng@vip.163.com (X.T.)
https://doi.org/10.1016/j.xcrm.2025.101978

SUMMARY

Accurate detection of malignant transformation in oral potentially malignant disorders (OPMDs) is crucial for guiding effective treatment and improving patient management. This study evaluates the potential of MET-binding peptide-indocyanine green (cMBP-ICG), a mesenchymal-epithelial transition factor (MET)-targeted near-infrared fluorescence imaging (NIRFI) probe, for biopsy site selection in OPMDs. Preclinical results demonstrate the superior accuracy of NIRFI-assisted biopsy over conventional oral examination (COE)-based biopsy in detecting high-grade dysplasia (HGD) or squamous cell carcinoma (SCC) and reducing missed detection rates. In a clinical trial with 50 patients, NIRFI-assisted biopsy achieves significantly higher diagnostic accuracy compared to COE-based biopsy (91% vs. 72%, $p = 0.0005$). These findings underscore the importance of NIRFI in enhancing diagnostic precision, supporting early detection and enabling timely and accurate treatment interventions for patients with OPMDs. The clinical trial is registered under the registration number ChiCTR2300074454.

INTRODUCTION

Oral potentially malignant disorders (OPMDs) are oral mucosal conditions with the potential to progress to oral squamous cell carcinoma (OSCC); the overall malignant transformation rate for OPMDs is 7.9%.[1] Presently, there is no effective method to prevent transformation of OPMDs to OSCC. Consequently, timely and accurate detection of malignant transformation of OPMDs is critical for improving prognosis. Notably, reported rates of early diagnosis of *in situ* OSCC are only 44%–55%.[2,3]

The method most employed for early detection of malignant transformation of OPMDs is conventional oral examination (COE)-based biopsy, which involves biopsy of suspected sites of disease under white light inspection and palpation. However, COE-based biopsy is highly subjective and relies heavily on the clinician's experience. Various auxiliary methods have been used to identify malignant progression of OPMDs, including vital staining, oral cytology, and light-based techniques, but none has demonstrated a significant improvement in diagnostic accuracy compared to COE-based examination.[4] Therefore, it is imperative

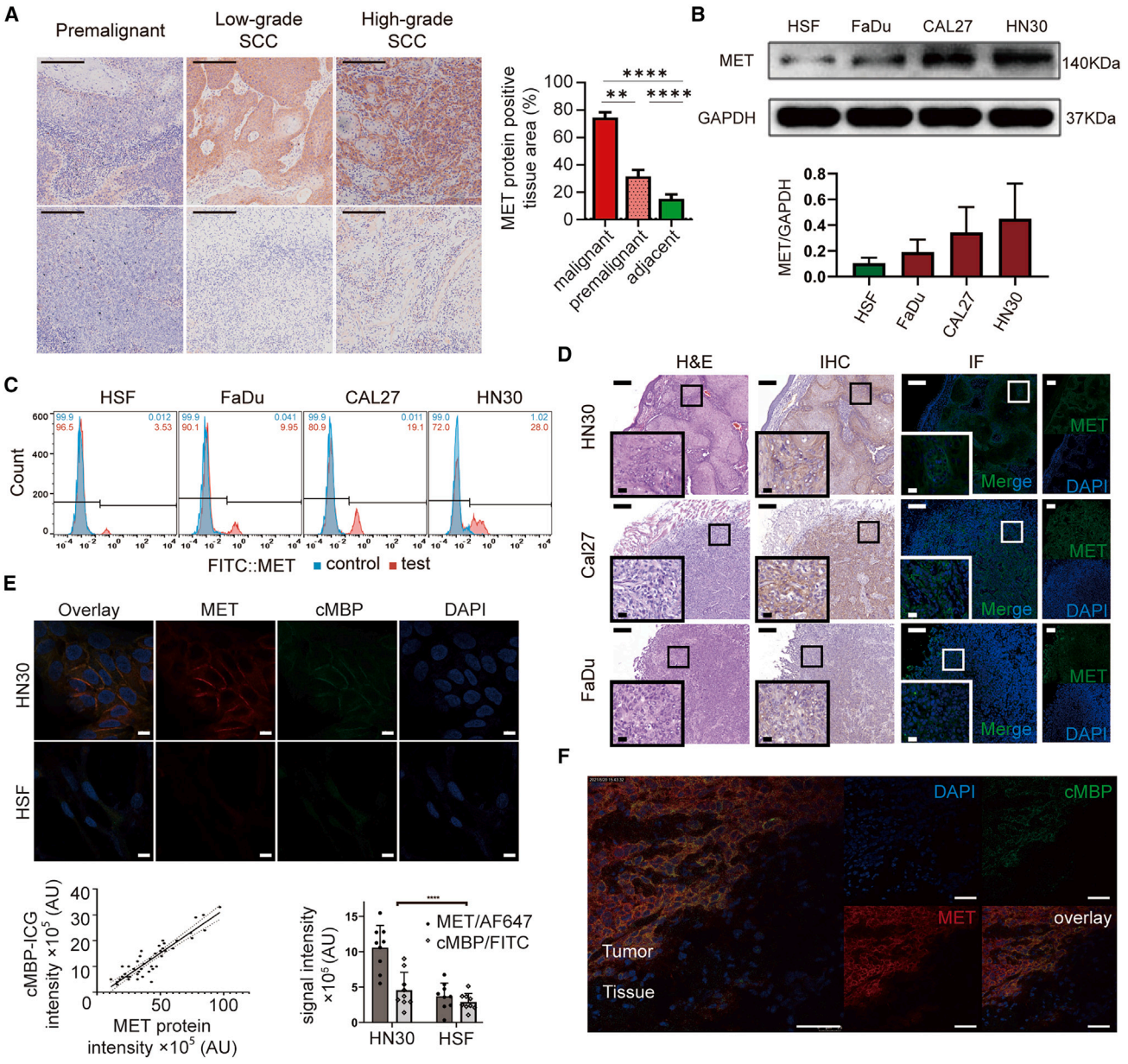

Figure 1. Verification of elevated MET expression in patient samples and orthotopic tumor tissues

(A) Immunohistochemical detection of MET using an anti-MET antibody in various grades of OSCC (top row) and adjacent normal epithelial tissues (bottom row). Brown: MET-positive tissue. Blue: hematoxylin counterstain. Bar graph, mean (SD) proportion of tissue area positive for MET expression was 74.50% (9.8%) in malignant tissues, 31.67% (14.8%) in premalignant tissues, and 15.11% (9.6%) in adjacent normal epithelial tissues. Malignant vs. premalignant, $p < 0.0001$; malignant vs. adjacent, $p < 0.0001$; premalignant vs. adjacent, $p = 0.0027$. Scale bars, 250 μm. *n* (specimens) = 9 biological replicates. Data are represented as mean ± SEM, with error bars shown only above the mean, analyzed using unpaired Student's t test. $^{**}p < 0.01$, $^{****}p < 0.0001$.

(B and C) (B) Western blot analysis of MET protein levels in cell lines FaDu, CAL27, and HN30 and control keratin epithelial cell line HSF (top). Bar graph quantification of MET expression (bottom). (C) Quantitative measurement of expression levels of FITC-conjugated MET in OSCC cell lines and control keratin epithelial cell line by flow cytometry. Data are represented as mean ± SEM, with error bars shown only above the mean. (B and C) *n* (HSF, CAL27, HN30, and FaDu) = 3 biological replicates.

(D) H&E staining (left), immunohistochemical detection (middle), and immunofluorescence (right) of MET expression in oral SCC orthotopic tumor tissues. Blue: DAPI-stained nuclei. Green: AF647-conjugated MET. The long horizontal scale bars correspond to 200 μm, while the short horizontal scale bars represent 20 μm. *n* (*ex vivo* sections) = 9 biological replicates.

(E) Localization of cMBP/FITC in HN30 and HSF cells via confocal imaging. Blue: DAPI-stained nuclei. Green: FITC-labeled cMBP. Red: AF647-conjugated anti-MET. Scale bars, 10 μm. Correlation in HN30 cells was evaluated with Pearson R-squared test. Pixel intensity of nine regions of interest from three cell slide pairs

(legend continued on next page)

to explore additional diagnostic adjuncts to enhance the early detection of OPMDs.

In recent years, optical techniques, such as near-infrared fluorescence imaging (NIRFI) following topical application of near-infrared fluorescence (NIRF) probes, have exhibited significant potential in diagnosing superficial solid tumors.[5,6] By applying probes targeting specific biomarkers to the mucosal surface and performing visual inspections using NIRFI, one can detect small mucosal lesions and achieve early cancer diagnosis, such as PARPi-FL for oral cancer detection[7] and IRdye800-antiCD44v6 for invasive bladder cancer detection.[8] Surface application of probes is rapid and noninvasive and particularly suitable for superficial lesions such as OPMDs.

Mesenchymal-epithelial transition factor (MET) plays a crucial role in tumorigenesis by activating the hepatocyte growth factor (HGF)/MET pathway, which triggers key signaling molecules such as protein kinase B (AKT) and mitogen-activated protein kinase.[9] This activation drives early tumor cell proliferation, survival, and invasion, marking the initial stages of cancer development.[10] Dysregulation of MET signaling is a significant factor in the onset of tumorigenesis, making it a critical target for preventing cancer initiation.[11] Notably, MET is overexpressed and aberrantly activated in over 80% of OSCC cases, compared to less than 30% in normal epithelial tissues,[12] highlighting its potential as a biomarker for early detection.[13,14] Our previously synthesized peptide-based NIRF dye, MET-binding peptide-indocyanine green (cMBP-ICG), has been demonstrated to specifically target OSCC by binding to MET, which enables the early detection of MET overexpression in the initial stages of OSCC development.[15]

The aim of this project was to determine whether cMBP-ICG-based NIRFI could improve the accuracy of biopsy site selection in OPMDs compared to COE. We first validated the expression levels of MET in different pathological tissue types using paraffin-embedded sections from biopsy specimens and surgical resection specimens from patients with OPMDs and OSCC. We then confirmed the *in vitro* and *in vivo* tumor-targeting capability of cMBP-ICG using OSCC cell lines and an orthotopic mouse model of OSCC. Further, we evaluated the utility of NIRFI with cMBP-ICG in biopsy site selection for OPMDs using the 4-nitroquinoline 1-oxide (4-NQO) mouse model. Subsequently, we conducted an exploratory clinical trial of NIRFI with cMBP-ICG involving 50 subjects with OPMDs.

RESULTS

Toxicity of cMBP-ICG

Statistical analysis revealed significant alterations in white blood cell count, lymphocyte and neutrophil proportions, and serum albumin and total cholesterol levels at 24 h and 14 days after cMBP-ICG administration and a significant alteration in hemoglobin level at 14 days. No significant differences were observed in the results of other routine blood and biochemical tests between before and after cMBP-ICG administration (Figure S1; Table S1)

MET expression in human tongue tumors and adjacent nonmalignant tissue

In all of the human tongue tumor specimens, immunohistochemical analysis showed that high levels of MET expression decisively distinguished tumor from normal tissue (Figure 1A). The percentage of tissue that stained positive for MET varied from 9.2% to 25.6% in normal tissue, whereas it varied from 23.0% to 82.0% in in precancerous tissue and cancerous tissue. The mean (SD) MET-positive area was 15.11% (9.6%) in nonmalignant tissue, 31.67% (14.8%) ($p = 0.0027$ vs. nonmalignant) in premalignant tissue, and 74.50% (9.8%) ($p < 0.0001$ vs. nonmalignant, $p < 0.0001$ vs. premalignant) in malignant tissue. On receiver operating characteristic (ROC) curve analysis, the best cutoff for separating tumor and normal tissue was found to be a 27.5% MET-positive area, which resulted in an area under the curve (AUC) of 0.9588, a sensitivity of 0.867, and a specificity of 0.933.

MET expression in cell lines

We previously proved the binding affinity between cMBP and MET.[15,16] To select the best cell line to study NIRFI with cMBP-ICG, we measured MET expression in OSCC cell lines: FaDu, CAL27, and HN30, which have high MET expression. Western blotting showed higher expression of MET in OSCCs than in HSF cells, while the difference between OSCCs was not significant (Figure 1B). Quantitative measurement of the expression levels of fluorescein isothiocyanate (FITC)-labeled MET in cells and HSF cells by flow cytometry showed MET positivity rates of 3.53% in HSF, 9.95% in FaDu, 19.1% in CAL27, and 28.0% in HN30 cells (Figure 1C). Thus, HN30 cells were chosen to build xenograft models of human MET-positive OSCC. H&E staining, immunohistochemistry staining, and immunofluorescence of *ex vivo* sections of these cell lines' subcutaneous tumor tissues showed regions with obvious positive findings compared to the findings in healthy tongue tissues (Figure 1D).

Colocalization of MET and cMBP in oral tumor tissue specimens

MET antibody staining colocalized with FITC-labeled cMBP fluorescence (Rcoloc. = 0.9145, $R^2 = 0.8363$; 95% confidence interval [CI] 0.84670.9531) (Figure 1E). cMBP not only displayed the quantity of MET present in a cell but also bound specifically to cells that express MET.

In vivo optical imaging after cMBP-ICG local injection in CDX

To check the targeting of cMBP-ICG *in vivo*, we injected cMBP-ICG into the edge of three mice tongues without neoplasms

analyzed with ImageJ. *n* (cell slides) = 3 biological replicates. Data are represented as mean ± SEM, with error bars shown only above the mean, analyzed using unpaired Student's t test. ****$p < 0.0001$.

(F) After intravenous injection of cMBP-ICG into OSCC nude mouse model, tumor tissues were harvested, frozen sections were prepared, and the distribution of MET in the frozen sections was assessed via immunofluorescence staining. Blue: DAPI-stained nuclei. Green: cMBP-ICG. Red: AF647-conjugated anti-MET. Scale bars, 50 μm. *n* (negative control group, cMBP-ICG injection group, and ICG injection group) = 3 biological replicates.

(negative control) and performed tumor imaging with a DPM-III-01 fluorescence stereoscope. In addition, six cell-derived xenografts (CAL27) were randomly divided into two groups. Group 1 (n = 3) was the cMBP-ICG intratumorally injection group, and group 2 (n = 3) was the ICG intratumorally injection group. Fluorescence imaging (Figure S2) demonstrated substantial cMBP-ICG and ICG aggregation in tongue regions damaged by cancer but no signal aggregation in tongues without tumors after cMBP-ICG injection. The mean tumor-to-background ratio (TBR) was 3.697 (1.568) in the cMBP-ICG group, 2.849 (0.798) in the ICG group, and 0.906 (0.267) in the negative control group. The TBRs differed significantly between the cell-derived xenograft groups and the negative control group (both $p < 0.0001$). In comparison, there was no difference in TBR between the cMBP-ICG group and the ICG group ($p = 0.4363$). Of note, under the condition of local injection, the difference in mean fluorescence intensity (MFI) between the cMBP-ICG group and the negative control group was similar to that between the ICG group and the negative control group (Figure S2A). This may be due to the short time between injection and imaging. A longer time may result in washout of nontarget small-molecular-weight probes, such as ICG, while target probes, such as cMBP-ICG, remain. Strong retention of the probe after local injection was confirmed by correlating the cMBP-ICG signal with H&E and immunohistochemical staining of tongue sections (Figure S2B). The results showed that cMBP-ICG was targeted to OSCC. Under the condition of a fluorescence microscope with a corresponding excitation/emission band, cMBP-ICG can be directly used for fluorescence imaging of frozen sections without additional staining steps. Fluorescence staining in frozen histological slices exhibited green fluorescence (cMBP-ICG) in tumor areas, and MET/AF647 confirmed that the cMBP-ICG-positive areas demonstrated overexpression of MET (Figure 1F).

Carcinogenesis and MET expression in 4-NQO-treated mice

In the analysis of carcinogenesis and MET expression in 4-NQO-treated mice (Figure 2A), pathological analysis of 15 slides from the 15 mice in the control group revealed no lesion, while 60 slides from the 15 mice in the test group revealed multiple lesions (Figure 2B), including 62 cases of low-grade dysplasia (LGD), 48 cases of high-grade dysplasia (HGD), 6 cases of carcinoma *in situ* (CIS), and 5 cases of invasive carcinoma (ICA) (Figure 2C). The distribution of these lesion types over time is illustrated in Figure 2D. The mean (SD) number of lesions per mouse was 1.00 (0.76) at 12 weeks, 1.87 (1.19) at 16 weeks, 2.33 (1.18) at 20 weeks, and 2.87 (1.36) at 24 weeks (Figure 2C). The number of lesions differed significantly between normal controls and those killed at 16 weeks, 20 weeks, and 24 weeks, as well as between the mice killed at 12 weeks and those killed at 24 weeks ($p < 0.0001$) and between the mice killed at 12 weeks and those killed at 20 weeks ($p < 0.01$). Comparisons between other groups did not show significant differences (Table S2).

Representative findings on immunohistochemistry to assess MET expression in different stages of OPMDs and OSCCs are shown in Figure 2E. The mean (SD) MET-positive proportion of the total lesion area ("MET-positive area") was 31.6% (12.3%) for LGD, 63.9% (18.5%) for HGD, 63.0% (13.7%) for CIS, and 80.0% (14.3%) for ICA (Figure 2F). Findings on pairwise comparisons among the different pathological types are summarized in Table S3. Relationships between time since 4-NQO treatment and MET-positive area, lesion diameter, and lesion type are summarized in Figure 2G.

The performance of MET-positive area as a classifier of dysplasia versus carcinoma and as a classifier of LGD versus HGD or OSCC was evaluated using ROC curves. For all slides, MET expression differentiated dysplasia from carcinoma with a specificity of 0.74, sensitivity of 0.82, and AUC of 0.82. MET expression differentiated LGD from HGD or later malignancy with a specificity of 0.83, sensitivity of 0.93, and AUC of 0.94 (Figure 2H).

Real-time NIRFI-assisted biopsy in the 4-NQO-induced OSCC mouse model

NIRFI in the 4-NQO-induced OSCC mouse model (Figures S3A and S3B) revealed greater fluorescence signal intensity in the neoplastic regions than in the adjacent uninvolved mucosa (Figure S3C). *Ex vivo* NIRFI demonstrated a mean (SD) TBR of 6.3 (2.7) for the HGD and SCC cases and 1.8 (1.3) for the normal epithelia and LGD cases ($p = 0.003$). *Ex vivo* NIRFI demonstrated an MFI of 17.4 (8.9) arbitrary units (a.u.) for the HGD and SCC cases and 3.5 (9.2) a.u. for the normal epithelia and LGD cases ($p = 0.0007$). NIRFI-assisted biopsy had greater accuracy than COE-based biopsy for detecting HGD or SCC (0.90 vs. 0.77; $p < 0.0001$) (Table 1).

In the 4-NQO-induced OSCC mouse model, the mean (SD) detection rate for HGD and OSCC was higher for NIRFI-assisted biopsy than for COE-based biopsy (0.66 [0.27] vs. 0.39 [0.25], $p = 0.002$), and the difference was particularly pronounced in the mice with biopsy at 24 weeks ($p < 0.0001$) (Table 2). The mean (SD) missed detection rate for HGD and OSCC was lower for NIRFI-assisted biopsy than for COE-based biopsy (0.01 [0.04] vs. 0.36 [0.2], $p < 0.0001$).

A multivariate logistic regression analysis indicated that, compared to COE-based biopsy, NIRFI-assisted biopsy was associated with a significantly lower HGD and carcinoma missed detection rate (OR = 0.024, $p < 0.001$) and significantly higher HGD and carcinoma (OR = 8.14, $p < 0.001$) and carcinoma (OR = 3.62, $p = 0.04$) detection rates (Table S4). Compared to the mice with biopsy at 20 weeks, the mice with biopsy at 24 weeks had significantly higher detection rates for HGD and carcinoma (OR = 1.36, $p = 0.01$) and carcinoma (OR = 1.38, $p = 0.04$). The ROC curves from the multivariate logistic regression analysis yielded an AUC of 0.80 for NIRFI-assisted biopsy ($p < 0.0001$), indicating high accuracy and statistical significance in the detection rates (Figure S4).

Clinical study of NIRFI-assisted biopsy for patients with OPMDs

Patient characteristics

From June through December 2023, 76 patients were assessed and 50 were enrolled and randomly assigned to the NIRFI-assisted biopsy group (25 patients; mean age 56.4 [SD 11.2] years; 11 men [44%]) or the COE-based biopsy group (25 patients; mean age 54.4 [SD 14.4] years; 9 men [36%]). Participant demographics and baseline characteristics were similar

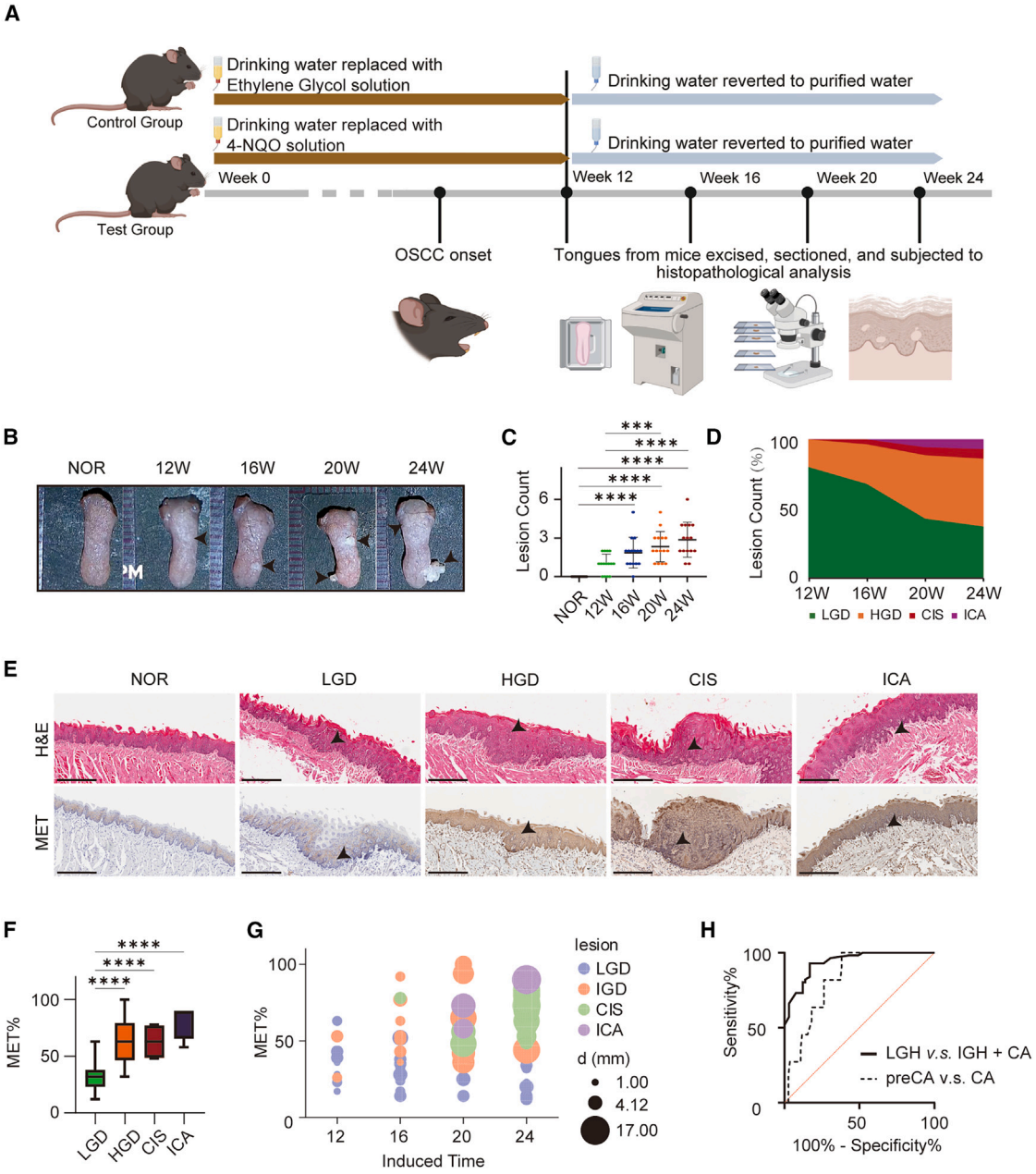

Figure 2. Lesion development and MET expression in the 4-NQO-induced OSCC mouse model

(A and B) (A) Overview of the experiments. Three mice from each group were killed at 0, 12, 16, 20, and 24 weeks. Tissue samples from the tongues of sacrificed mice were collected and subjected to histopathological examination after magnetic resonance imaging. (B) Typical presentations of tongue lesions in mouse model at different times after 4-NQO initiation. NOR, normal controls; W, weeks. (A and B) *n* (control) = 15, *n* (4-NQO-treated mice) = 15 biological replicates.

(C) Number of lesions of different pathological types at various times after 4-NQO initiation. Data are represented as mean ± SEM, analyzed using unpaired Student's t test. ***$p < 0.001$, ****$p < 0.0001$.

(D) Distribution of lesions of different pathological types at different times after 4-NQO initiation. W, weeks.

(E) H&E staining (top) and immunohistochemistry staining (bottom) of lesions of different pathological types. NOR, normal controls. Scale bars, 300 μm.

(F) Percentage of lesion area positive for MET for lesions of different pathological types. Data are represented as mean ± SEM, analyzed using unpaired Student's t test. ****$p < 0.0001$.

(G) Percentage of lesion area positive for MET, lesion diameter, and distribution of lesions of different pathological types at different times after initiation of 4-NQO.

(H) Receiver operating characteristic (ROC) curves evaluating the performance of MET-positive area as a classifier.

(C–H) *n* (lesions) = 121 biological replicates.

Table 1. Diagnostic performance of NIRFI-assisted biopsy and COE-based biopsy in mouse tongue lesions

	NIRFI-assisted biopsy			COE-based biopsy		
	20 weeks	24 weeks	Combined	20 weeks	24 weeks	Combined
Sensitivity	0.87	0.79	0.86	0.65	0.50	0.59
Specificity	0.82	0.89	0.93	0.82	0.89	0.89
PPV	0.69	0.83	0.89	0.63	0.75	0.79
NPV	0.93	0.86	0.91	0.84	0.72	0.76
Accuracy	0.84	0.85	0.90	0.77	0.73	0.77

COE, conventional oral examination; NIRFI, near-infrared fluorescence imaging; NPV, negative predictive value; PPV, positive predictive value. A positive test result is defined as a lesion with a pathological diagnosis of high-grade dysplasia (HGD) or squamous cell carcinoma (SCC). A negative test result is defined as a lesion with a pathological diagnosis of normal epithelial tissue or low-grade dysplasia (LGD).

between the groups (Table S5). Age, biopsy type (COE-based vs. NIRFI-assisted), and baseline oral fluorescence signal intensity were similar between the pathologically positive (HGD or OSCC) and pathologically negative (normal epithelium or LGD) groups (Table S6).

Diagnostic accuracy

Each patient had two biopsy sites selected, one was based on COE and the other on the basis of NIRFI, for a total of 100 selected biopsy sites (Figure 3). In 46 of the 50 patients, the two biopsy sites were concordant.

Based on NIRFI, 65 biopsy sites were classified as negative (normal epithelium or LGD) and 35 were classified as positive (HGD or OSCC); based on COE, 50 biopsy sites were classified as negative and 50 were classified as positive. Final pathological results were negative for 64 biopsy sites and positive for 36 biopsy sites. Representative fluorescence images of patients are shown in Figure 4A. The MFI and TBR for all biopsy sites are presented in Figure 4B. The diagnostic performance of NIRFI-assisted biopsy and COE-based biopsy is presented in Table 3. Figure 4C presents two cases where the biopsy sites selected by NIRFI and COE did not align. NIRFI-assisted biopsy demonstrated higher accuracy, sensitivity, specificity, positive predictive value, and negative predictive value. ROC curves were generated for both groups (Figure 4D) and showed AUCs of 0.91 for the NIRFI-assisted biopsy group and 0.71 for the COE-based biopsy group.

Quantification of cMBP-ICG fluorescence

For the pathologically negative and pathologically positive groups, respectively, mean (SD) cMBP-ICG fluorescence values were as follows: pre-wash MFI, 72 (42) a.u. and 106 (48) a.u. (p = 0.01); after-wash MFI, 47 (48) a.u. and 70 (50) a.u. (p = 0.12); pre-wash TBR, 1.2 (0.56) and 1.7 (0.55 (p = 0.002); and after-wash TBR, 1.3 (1.1) and 2.9 (0.99 (p < 0.0001) (Figure 4E). ROC curves for distinguishing between pathologically negative and positive lesions using four different indicators are shown in Figure 4F. The AUC for pre-wash MFI was 0.55 with a cutoff value of 93.13 a.u. (sensitivity: 0.68, specificity: 0.66). The AUC for pre-wash TBR was 0.63 with a cutoff value of 1.23 a.u. (sensitivity: 0.95, specificity: 0.49). The AUC for after-wash MFI was 0.72 with a cutoff value of 38.43 (sensitivity: 0.74, specificity: 0.60). The AUC for after-wash TBR was 0.93 with a cutoff value of 1.59 (sensitivity: 1.00, specificity: 0.86). Using these four indicators to establish a logistic regression diagnostic model resulted in an overall AUC of 0.78 (sensitivity: 0.80, specificity: 0.75).

Safety

Following cMBP-ICG fluorescence imaging, no patient experienced anaphylaxis or local irritation or discomfort.

DISCUSSION

In this study, we confirmed that MET-positive OSCC cells preferentially absorbed the peptide-based NIRF probe cMBP-ICG. We further confirmed that the targeted smear-based fluorescent probes can accurately determine the degree of epithelial dysplasia and identify suspicious OSCC lesions, regardless of specific diseases. This improves the early detection rate of early tumors. Therefore, this study provides a modular and flexible approach for different screening and exclusion goals of OSCC in various scenarios, potentially offering a convenient and safe new detection method to improve the early diagnosis rate of OSCC.

NIRFI has high sensitivity, uses non-ionizing radiation, and has simple operation and low cost, characteristics that make NIRFI particularly suitable for real-time clinical imaging. Handheld real-time NIRFI devices for head and neck cancer have gradually matured, and some of them have entered the stage of clinical trials.[17,18] NIRFI can detect tissue signals up to a depth of 5–6 mm. Given that OSCC arises from squamous cells on the surface of oral mucosa, NIRFI is optimal for early detection of OSCC lesions. Furthermore, incorporating a targeting element specific to tumor molecular markers can significantly enhance the diagnostic performance of NIRFI. MET-targeted NIRFI offers a practical, noninvasive tool for early detection of OSCC, well suited to outpatient settings and large-scale screening. Its molecular specificity allows for real-time biopsy, accurately marks high-risk lesions, minimizes the need for extensive biopsy sampling, and reduces patient discomfort. With its straightforward operation, NIRFI requires minimal clinical training and may help streamline diagnostic workflows. This technique's sensitivity to MET expression in OSCC may also provide a targeted approach that is both cost-effective and highly accessible, improving efficiency in cancer detection and intervention. Therefore, targeted NIRFI can assist in achieving clinical accuracy by providing "real-time illumination" of early suspicious OSCC nests at the millimeter level to guide clinical biopsy. This is a feasible approach for achieving early cancer intervention and improving prognosis.

The current experiment's merit lies in establishing a practical imaging protocol for OPMDs. Prior to this study, various

Table 2. Missed detection rates and detection rates of NIRFI-assisted biopsy and COE-based biopsy in mouse tongue OPMDs and carcinomas

Lesion type and time since start of 4-NQO		NIRFI-assisted biopsy	COE-based biopsy	*p* value
Missed detection rates				
HGD and carcinoma		–	–	–
–	20 weeks	0.02 ± 0.05	0.36 ± 0.20	0.001
	24 weeks	0	0.37 ± 0.20	<0.0001
	Combined	0.01 ± 0.04	0.36 ± 0.20	<0.0001
Carcinoma		–	–	–
–	20 weeks	0.20 ± 0.06	0.09 ± 0.10	0.19
	24 weeks	0	0.02 ± 0.06	0.33
	Combined	0.01 ± 0.04	0.05 ± 0.10	0.11
Detection rates				
HGD and carcinoma		–	–	–
–	20 weeks	0.48 ± 0.22	0.31 ± 0.10	0.21
	24 weeks	0.85 ± 0.18	0.46 ± 0.10	<0.0001
	Combined	0.66 ± 0.27	0.39 ± 0.25	0.002
Carcinoma		–	–	–
–	20 weeks	0.37 ± 0.26	0.39 ± 0.10	0.94
	24 weeks	0.39 ± 0.17	0.40 ± 0.15	0.95
	Combined	0.39 ± 0.19	0.40 ± 0.13	0.92

4-NQO, 4-nitroquinoline 1-oxide; COE, conventional oral examination; HGD, high-grade dysplasia; NIRFI, near-infrared fluorescence imaging; OPMDs, oral potentially malignant disorders. Values in table are mean ± SD unless otherwise indicated.

methods were employed to enhance the precision of OPMD examination, including vital stains like toluidine blue, oral cytology (Oral CDx brush biopsy), light-based detection systems (e.g., ViziLite and VELscope), oral spectroscopy, and analyses of blood and saliva. Although these methods have their own advantages and disadvantages, the main drawback lies in the instability of the results and the alteration of the lesion morphology.[4,19,20] In contrast, the fluorescent examination used in this study offers unique benefits. For instance, in comparison to cytological examination, early identification and excision of high-risk oral leukoplakia can significantly decrease the likelihood of malignant transformation. Unlike with vital staining, with fluorescent staining, the morphology and color of the lesion itself remain unchanged. The different imaging outcomes of the lesion under two light sources can be separately observed through inspection with the naked eye and NIRFI display screen analysis.

Use of the 4-NQO-induced OSCC mouse model is another advantageous feature of this study. Previous studies that relied on biopsy sampling lacked data on false negatives and false positives due to a lack of pathological verification in areas judged to be negative by the sampling doctor.[21] In our current study, we employed an animal model to perform histopathological examination of 5-μm paraffin sections from the remaining tongue that was not sampled, enabling detection of any lesions missed by the two sampling methods and ensuring more comprehensive and reliable results.

In our prospective randomized controlled trial using topical application of the targeted fluorescent imaging probe cMBP-ICG for identification of malignant transformation from OPMD to OSCC, we found that cMBP-ICG fluorescence achieved favorable accuracy. Until now, the early diagnosis of OSCC has mainly relied on the clinician's visual inspection to determine the necessity of a biopsy and select an appropriate biopsy site. Our study provided preliminary evidence that cMBP-ICG fluorescence imaging can significantly enhance the ability to differentiate between benign and malignant lesions, thereby improving the efficacy of biopsy procedures.

In this study, the classification of cases as pathologically negative or positive was based on the corresponding clinical intervention strategy. In patients with oral epithelial dysplasia, the rate of malignant transformation is approximately 12.1%.[22] A longitudinal study further revealed that the rates of malignant transformation for mild, moderate, and severe dysplasia were 8.1%, 16.1%, and 38.5%, respectively.[23] Therefore, in cases of mild dysplasia, clinicians typically adopt a follow-up approach, while in cases of moderate to severe epithelial dysplasia, surgical excision is performed.[24] Thus, we defined pathologically negative as OPMD or mild dysplasia.

The process of malignant transformation of OPMDs is slow and insidious, initially manifesting only as cytological changes. The histopathological results obtained from biopsy are regarded as the criterion standard in managing OPMDs.[25] Therefore, it is crucial to optimize the timing and location of the biopsy. Precise assessment of lesions can prevent unnecessary invasive procedures, enhance the accuracy of biopsies, avert missed or delayed diagnoses, and ensure timely intervention for patients.

At present, none of the adjunctive tests, including vital staining, oral cytology, and light-based and combined tests, are adequate substitutes for biopsy and histological assessment.[4] We attempted to use targeted fluorescence imaging to improve the specificity of fluorescent attachment and to minimize nonspecific attachment by gargling. In fluorescence imaging, we can obtain morphological information beyond what can be observed with the naked eye. The information arises from changes at the molecular level, which are related to the MET expressed by tumor cells. During the subjective process of identifying high-risk lesions using real-time cMBP-ICG fluorescence imaging, researchers integrated various characteristics, such as quantifying the disparity between suspicious sites and surrounding mucosa, assessing signal uniformity, and evaluating the smoothness of lines within high signal areas. Our study showed that NIRFI with cMBP-ICG achieved a diagnostic accuracy of 91% and a specificity of 93%, accurately identifying lesions as pathologically negative that had initially been diagnosed as positive, thus reducing the occurrence of false positives by three-quarters. These findings indicate that cMBP-ICG fluorescence imaging has higher accuracy than COE in identifying high-risk lesions and assists in the biopsy of OPMDs.

To ensure consistency across patients, we used hard palate fluorescence as a baseline reference to control individual variability in fluorescence signals due to differences in oral mucosa. However, the factors such as oral hygiene, mucosal texture, and MET expression levels may still impact signal variability,

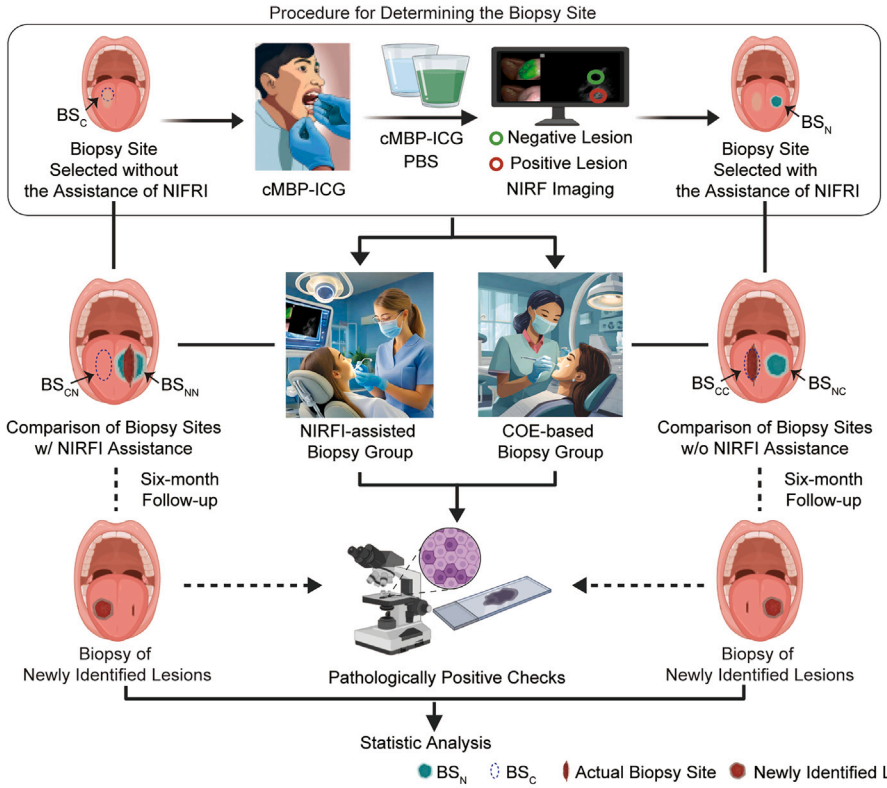

	Subject NO.		Pathology Results	Performance Metrics ① Diagnosis +	Performance Metrics ① Diagnosis -	Follow-up Lesion	Performance Metrics ② Diagnosis +	Performance Metrics ② Diagnosis -
NIRFI-assisted Biopsy	①	BS_{NN} aligned with BS_{CN}	+	TP_{NIRFI} TP_{COE}	FN_{NIRFI}	/	/	/
			-	FP_{NIRFI} FP_{COE}	TN_{NIRFI}	/	/	/
	① ②	BS_{NN} misaligned with BS_{CN}	+	TP_{NIRFI}	FN_{NIRFI} FN_{COE}	/	/	/
			-	FP_{NIRFI}	TN_{NIRFI} TN_{COE}	Newly Identified	TP_{COE}	FN_{NIRFI}
						Non	FP_{COE}	TN_{NIRFI}
COE-based Biopsy	①	BS_{CC} aligned with BS_{NC}	+	TP_{NIRFI} TP_{COE}	FN_{NIRFI}	/	/	/
			-	FP_{NIRFI} FP_{COE}	TN_{NIRFI}	/	/	/
	① ②	BS_{CC} misaligned with BS_{NC}	+	TP_{COE}	FN_{NIRFI}	/	/	/
			-	FP_{COE}	TN_{NIRFI}	Newly Identified	TP_{NIRFI}	FN_{NIRFI} FN_{COE}
						Non	FP_{NIRFI}	TN_{NIRFI} TN_{COE}

Figure 3. Design of the clinical trial

Patients with OPMDs underwent visual inspection and NIRFI examination of the oral cavity prior to biopsy. First, an oral mucosal specialist independently selected the most appropriate biopsy site (BS_C) based on visual inspection without reference to NIRFI, documented the biopsy site with photos, and assigned a clinical diagnosis. Next, an NIRFI operator selected the most appropriate biopsy site with NIRFI assistance (BS_N), captured key frames, and marked the site directly on the images, which were then documented along with the clinical diagnosis. Subsequently, patients in the NIRFI-assisted biopsy group underwent biopsy at BS_N, while subjects in the COE-based biopsy group underwent biopsy at BS_C. Six months after biopsy, all patients were re-examined visually to check for new lesions, and any newly identified lesions were biopsied using the biopsy method used previously. All biopsy tissues were paraffin embedded and H&E stained and categorized as negative (normal epithelium, LGD) or positive (HGD, SCC). BS_{NN}, NIRFI-assisted biopsy sites in the NIRFI-assisted biopsy group; BS_{CN}, specialist-selected biopsy sites without NIRFI in the NIRFI-assisted biopsy group; BS_{CC}, specialist-selected biopsy sites without NIRFI in the COE group; BS_{NC}, NIRFI-assisted biopsy sites in the COE-based biopsy group; FN, false negative; FP, false positive; TN, true negative; TP, true positive. Subscript *NIRFI* indicates the NIRFI-assisted biopsy group, and subscript *COE* indicates the COE-based biopsy group.

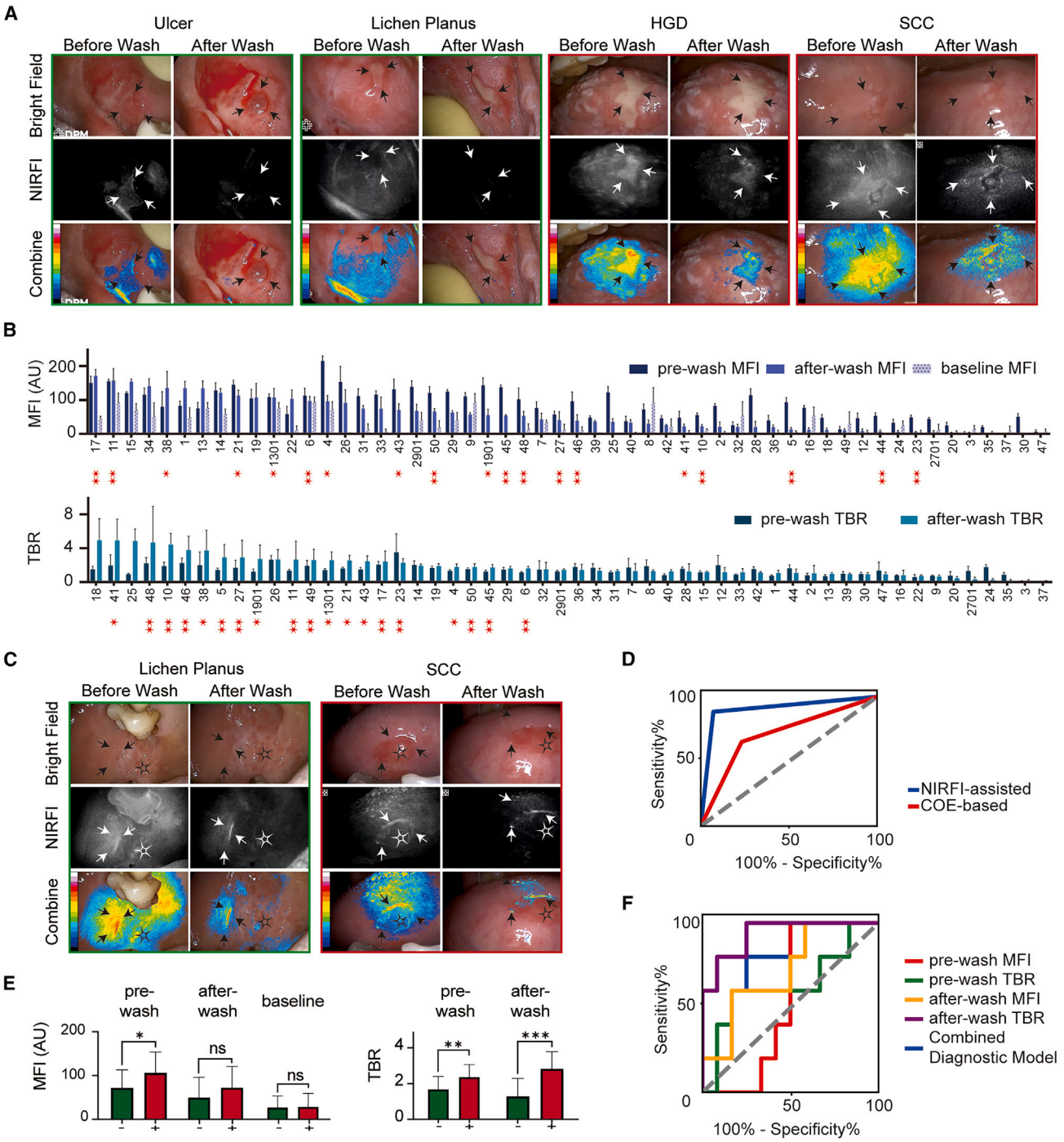

Figure 4. Clinical cMBP-ICG fluorescence imaging of OPMDs

(A) Representative bright-field images (top), black and white NIRFI images (middle), and combined pseudo-color fluorescence and bright-field images (bottom) of biopsy sites. The left two panels depict typical imaging findings for pathologically negative cases (ulcer and lichen planus), while the right two panels depict typical imaging findings for pathologically positive cases (HGD and SCC). Before the wash step, fluorescence signals were similar in all four panels due to physical attachment of cMBP-ICG. After the wash step, non-targeted cMBP-ICG is removed, and fluorescence signals are higher in pathologically positive cases than in pathologically negative cases.

(B) Pre-wash, after-wash, and baseline palate MFI and TBR for all cases, arranged in descending order of after-wash MFI (top row) and TBR (bottom row). No asterisk: pathologically negative. One asterisk: HGD. Two asterisks: SCC.

(C) Representative bright-field images (*top*), black and white NIRFI images (*middle*), and combined pseudo-color fluorescence and bright-field images (*bottom*) from cases with differing biopsy sites as determined by NIRFI and COE. Arrows: NIRFI-assisted biopsy sites. Stars: COE-based biopsy sites.

(legend continued on next page)

indicating the need for further refinement in standardization techniques to enhance the reliability and reproducibility of our imaging results.

Our analysis showed significant TBR variability between male and female patients (data not shown), with a higher fluorescence at lesion margins in males, which may potentially indicate a greater lesion dispersion. Such differences may align with reports of gender-based disparities in biomarkers influencing tumor behavior and imaging metrics.[26] These findings might highlight the importance of gender as a variable for improvement of diagnostic consistency.

Consequently, individual differences in oral status could influence the quantification of fluorescence results. This discrepancy may be attributed to interindividual variations in physical adsorption capacity of fluorescent agents and baseline MET expression among patients with diverse oral conditions. However, by comparing the MFI of the lesion site with that of the surrounding normal mucosa, it was possible to estimate the risk level of the lesions. Therefore, TBR may be more useful than MFI in distinguishing low-risk and high-risk lesions.

In addition, our randomized controlled trial was designed with particular attention to the difficulty in selecting biopsy sites due to the often-large-size OPMD lesions. We found that at least 50% of the patients in the trial had OPMDs exceeding an area of 1 square centimeter, posing challenges for clinicians in selecting appropriate biopsy sites. In the COE group, we observed a patient with initially negative biopsy histological results. However, within 3 months of follow-up, the wound exhibited erosion, and subsequent diagnosis revealed moderately differentiated SCC necessitating surgical intervention. Therefore, accurate selection of the most suitable biopsy site can permit timely diagnosis of patients who need intervention. We used the cMBP-ICG fluorescence imaging results as the basis for biopsy sampling in the experimental group and explored the value of fluorescence for biopsy guidance. The results indicate that cMBP-ICG fluorescence imaging has the potential to enhance diagnostic specificity, reduce surgeon errors in site selection, and improve biopsy accuracy and effectiveness. For general stomatology departments, fluorescence imaging may offer a greater enhancement in diagnostic efficiency.

Although our current study found that the 4-NQO-induced OSCC mouse model effectively simulated the carcinogenesis, it has certain limitation. The tumors predominantly formed on the dorsum of the tongue were different from the lateral locations typically seen in human patients,[27,28] which may impact translational relevance. While our clinical trial demonstrated the feasibility and diagnostic potential of MET-targeted NIRFI, the relatively small sample size limits the generalizability of these findings and restricts further subgroup analysis. Therefore, larger prospective and more diverse studies are needed to confirm our findings. Lastly, although no adverse events were noted, further evaluation of long-term safety with repeated probe applications remains needed to assess the potential influence by probe accumulation in tissues, immune responses of patient tolerance, and localized tissue mild inflammation effects.

In conclusion, this study developed a fluorescent dye, cMBP-ICG, and utilized a 4-NQO-induced mouse model of spontaneous OSCC to successfully replicate the progression of OPMDs to OSCC. By incorporating cMBP-ICG with a real-time NIRFI platform for biopsy assistance, the detection accuracy of early precancerous lesions was elevated from 77% to 90%. NIRFI-assisted biopsy outperformed COE-based biopsy in detecting HGD and exhibited a higher detection rate and a lower missed detection rate. In the preliminary exploratory clinical trial in patients with OPMDs, the most appropriate biopsy sites indicated by NIRFI matched the most appropriate biopsy sites indicated by COE, and NIRFI clearly delineated lesions. These results suggest that NIRFI with cMBP-ICG has the potential to offer a novel noninvasive real-time method to guide biopsy sampling. Ultimately, this approach may revolutionize current clinical diagnosis and treatment protocols for OPMDs, leading to an improved early detection rate of OSCC. Furthermore, theoretically, this approach may also be applicable to any other superficial tumor that follows its own progression process and involves critical biomarkers. To support the broader clinical adoption of MET-targeted NIRFI, future directions should focus on optimizing setup of requirements to enhance operator training and refine imaging standardization procedures.

Limitations of the study

The study has several limitations. Firstly, the 4-NQO-induced OSCC mouse model exhibits translational limitations, as tumors primarily form on the dorsum of the tongue, differing from the lateral sites commonly observed in human patients. Future studies could incorporate alternative models, such as orthotopic tumor implantation in lateral tongue sites, or advanced immunodeficient models like non-obese diabetic/severe combined immunodeficiency mice, to better mimic human OSCC. Secondly, the relatively small sample size of the clinical trial limits generalizability and restricts subgroup analyses. For instance, significant TBR variability was observed between male and female patients, with higher fluorescence at lesion margins in males, potentially indicating greater lesion dispersion. Such gender-based differences may impact diagnostic consistency and warrant further investigation. However, due to the limited dataset, further analyses could not be performed to confirm these observations, leaving this as a hypothesis rather than a definitive conclusion. Larger, multicenter studies are needed to validate these findings and explore how demographic factors and lesion characteristics influence diagnostic performance. Finally, the long-term safety of repeated probe applications remains uncertain. Potential risks, such as tissue accumulation, immune responses, and localized

(D) Comparison of MFI and TBR between the pathologically negative (green) and pathologically positive (red) groups.
(E) ROC curves for NIRFI-assisted biopsy and COE-based biopsy in distinguishing pathologically negative and pathologically positive OPMDs. Data are represented as mean ± SEM, with error bars shown only above the mean, analyzed using unpaired Student's t test. $^{*}p < 0.05$, $^{**}p < 0.01$, $^{***}p < 0.001$; ns, not significant.
(F) Multivariable ROC curve analysis for different methods of distinguishing pathologically negative and pathologically positive OPMDs.
(A–F) *n* (participants) = 50 biological replicates. *n* (selected biopsy sites) = 100 technical replicates.

Table 3. Diagnostic performance of NIRFI-assisted biopsy and COE-based biopsy in patients with OPMDs

	NIRFI-assisted biopsy	COE-based biopsy	*p* value
Accuracy	0.91 (0.83, 0.95)	0.72 (0.62, 0.80)	0.0005
Sensitivity	0.88 (0.81, 0.93)	0.65 (0.55, 0.74)	0.0001
Specificity	0.93 (0.86, 0.96)	0.76 (0.68, 0.84)	0.002
PPV	0.90 (0.83, 0.95)	0.68 (0.59, 0.77)	0.0001
NPV	0.91 (0.84, 0.95)	0.74 (0.64, 0.82)	0.001

COE, conventional oral examination; NIRFI, non-infrared fluorescent imaging; NPV, negative predictive value; OPMDs, oral potentially malignant disorders; PPV, positive predictive value.
Values in parentheses are 95% CIs. A positive test result is defined as a lesion with a pathological diagnosis of high-grade dysplasia (HGD) or squamous cell carcinoma (SCC). A negative test result is defined as a lesion with a pathological diagnosis of normal epithelial tissue or low-grade dysplasia (LGD).

inflammation, require further investigation. Longitudinal studies and repeated-dose experiments are essential to ensure clinical safety and feasibility.

RESOURCE AVAILABILITY

Lead contact

Requests for further information and resources should be directed to and will be fulfilled by the lead contact, Xiaofeng Tao (cjr.taoxiaofeng@vip.163.com).

Materials availability

There are restrictions to the availability of cMBP-ICG due to the lack of an external centralized repository for its distribution and our need to maintain the stock. We are glad to share cMBP-ICG with reasonable compensation by requester for its processing and shipping.

Data and code availability

- The datasets generated during this study are included in the manuscript and supplementary materials.
- No new code was created or used in this study.
- Any additional information required to reanalyze the data reported in this work paper is available from the lead contact upon request

ACKNOWLEDGMENTS

We thank Professor Qifan Yan (East China University of Science and Technology) for advice on optical imaging techniques and Researcher Jingya Sun (Shanghai Institute of Materia Medica, Chinese Academy of Sciences) for guidance on preclinical experiments. We also appreciate the contributions of Jun Wu, Yuan Yuan, Yunjing Zhu, Rui Wang, Qi Fan, Gongxin Yang, and Jiliang Ren to the early stages of this research. This work was supported by the National Natural Science Foundation of China (grant nos. 82172049 and 82172051), the Clinical Research Program of Shanghai Ninth People's Hospital, Shanghai Jiao Tong University School of Medicine (grant no. JYLJ202205), the Shanghai Municipal Commission of Health and Family Planning (grant no. 172), the Medical-Engineering Cross-Research Fund (grant no. YG2024QNA 23), and the Cross-disciplinary Research Fund of Shanghai Ninth People's Hospital (JYJC202304).

DECLARATION OF INTERESTS

The authors have a related patent "Near-infrared fluorescence imaging agent targeting c-Met and its use" filed by X.T. et al., Shanghai Ninth People's Hospital, China, 2022 (patent number 202210118240.6).

AUTHOR CONTRIBUTIONS

Conceptualization, J.W., X.S., Y.Y., and X.T.; methodology, R.H., C. Zhan, Z.C., K.W., and J.T.; investigation, J.W., X.S., Q.M., L.Y., X.Z., L.W., J.C., C. Zhang, S.L., R.H., K.W., and J.T.; data curation, Q.M. and L.Y.; formal analysis, G.L. and N.G.; software, K.W. and J.T.; visualization, J.W.; writing – original draft, J.W. and Q.M.; writing – review and editing, G.L., Y.Y., and X.T.; funding acquisition J.W., Y.Y., and X.T.; resources, X.S.; supervision, Y.Y. and X.T.

DECLARATION OF GENERATIVE AI AND AI-ASSISTED TECHNOLOGIES

During the preparation of this work, the authors used Adobe Firefly to create illustrations for Figure 3, including the COE part, NIRFI-assisted biopsy group, and COE-based biopsy group, to clarify the clinical trial procedures for broader readers. After using this tool, the authors reviewed and edited the content as needed and take full responsibility for the content of the publication.

STAR★METHODS

Detailed methods are provided in the online version of this paper and include the following:

- KEY RESOURCES TABLE
- EXPERIMENTAL MODEL AND STUDY PARTICIPANT DETAILS
  - Animal models
  - Cell lines and cell culture
  - Human participants
- METHOD DETAILS
  - Synthesis and characterization of cMBP-ICG
  - *In vivo* toxicological evaluation of cMBP-ICG
  - Confocal and light microscopy imaging
  - Western blotting
  - Flow cytometry
  - NIRFI with cMBP-ICG to identify OSCC in CDXs
  - Tumors and MET expression in the 4-NQO model
  - NIRFI to identify OPMD in the 4-NQO model
  - Exploratory clinical trial
- QUANTIFICATION AND STATISTICAL ANALYSIS
- ADDITIONAL RESOURCES

SUPPLEMENTAL INFORMATION

Supplemental information can be found online at https://doi.org/10.1016/j.xcrm.2025.101978.

Received: September 16, 2024
Revised: November 26, 2024
Accepted: January 28, 2025
Published: February 24, 2025

REFERENCES

1. Warnakulasuriya, S., Kujan, O., Aguirre-Urizar, J.M., Bagan, J.V., González-Moles, M.Á., Kerr, A.R., Lodi, G., Mello, F.W., Monteiro, L., Ogden, G.R., et al. (2021). Oral potentially malignant disorders: A consensus report from an international seminar on nomenclature and classification, convened by the WHO Collaborating Centre for Oral Cancer. Oral Dis. *27*, 1862–1880. https://doi.org/10.1111/odi.13704.
2. Seoane, J., Alvarez-Novoa, P., Gomez, I., Takkouche, B., Diz, P., Warnakulasiruya, S., Seoane-Romero, J.M., and Varela-Centelles, P. (2016). Early oral cancer diagnosis: The Aarhus statement perspective. A systematic review and meta-analysis. Head Neck *38*, E2182–E2189. https://doi.org/10.1002/hed.24050.
3. Nieminen, M., Aro, K., Mäkitie, A., Harlin, V., Kainulainen, S., Jouhi, L., and Atula, T. (2021). Challenges in diagnosing head and neck cancer in primary

health care. Ann. Med. *53*, 26–33. https://doi.org/10.1080/07853890.2020.1802060.

4. Walsh, T., Macey, R., Kerr, A.R., Lingen, M.W., Ogden, G.R., and Warnakulasuriya, S. (2021). Diagnostic tests for oral cancer and potentially malignant disorders in patients presenting with clinically evident lesions. Cochrane Database Syst. Rev. *7*, CD010276. https://doi.org/10.1002/14651858.CD010276.pub3.
5. Zhang, Z., Du, Y., Shi, X., Wang, K., Qu, Q., Liang, Q., Ma, X., He, K., Chi, C., Tang, J., et al. (2024). NIR-II light in clinical oncology: opportunities and challenges. Nat. Rev. Clin. Oncol. *21*, 449–467. https://doi.org/10.1038/s41571-024-00892-0.
6. Hu, Z., Chen, W.-H., Tian, J., and Cheng, Z. (2020). NIRF Nanoprobes for Cancer Molecular Imaging: Approaching Clinic. Trends Mol. Med. *26*, 469–482. https://doi.org/10.1016/j.molmed.2020.02.003.
7. Demétrio De Souza França, P., Kossatz, S., Brand, C., Karassawa Zanoni, D., Roberts, S., Guru, N., Adilbay, D., Mauguen, A., Valero Mayor, C., Weber, W.A., et al. (2021). A phase I study of a PARP1-targeted topical fluorophore for the detection of oral cancer. Eur. J. Nucl. Med. Mol. Imag. *48*, 3618–3630. https://doi.org/10.1007/s00259-021-05372-6.
8. Shang, W., Peng, L., He, K., Guo, P., Deng, H., Liu, Y., Chen, Z., Tian, J., and Xu, W. (2022). A clinical study of a CD44v6-targeted fluorescent agent for the detection of non-muscle invasive bladder cancer. Eur. J. Nucl. Med. Mol. Imag. *49*, 3033–3045. https://doi.org/10.1007/s00259-022-05701-3.
9. Knowles, L.M., Stabile, L.P., Egloff, A.M., Rothstein, M.E., Thomas, S.M., Gubish, C.T., Lerner, E.C., Seethala, R.R., Suzuki, S., Quesnelle, K.M., et al. (2009). HGF and c-Met Participate in Paracrine Tumorigenic Pathways in Head and Neck Squamous Cell Cancer. Clin. Cancer Res. *15*, 3740–3750. https://doi.org/10.1158/1078-0432.ccr-08-3252.
10. Saintigny, P., William, W.N., Foy, J.-P., Papadimitrakopoulou, V., Lang, W., Zhang, L., Fan, Y.H., Feng, L., Kim, E.S., El-Naggar, A.K., et al. (2018). Met Receptor Tyrosine Kinase and Chemoprevention of Oral Cancer. J. Natl. Cancer Inst. *110*, 250–257. https://doi.org/10.1093/jnci/djx186.
11. Lim, Y.C., Kang, H.J., and Moon, J.H. (2014). C-Met pathway promotes self-renewal and tumorigenecity of head and neck squamous cell carcinoma stem-like cell. Oral Oncol. *50*, 633–639. https://doi.org/10.1016/j.oraloncology.2014.04.004.
12. Seiwert, T.Y., Jagadeeswaran, R., Faoro, L., Janamanchi, V., Nallasura, V., El Dinali, M., Yala, S., Kanteti, R., Cohen, E.E.W., Lingen, M.W., et al. (2009). The MET receptor tyrosine kinase is a potential novel therapeutic target for head and neck squamous cell carcinoma. Cancer Res. *69*, 3021–3031. https://doi.org/10.1158/0008-5472.CAN-08-2881.
13. Liang, M., Yang, M., Wang, F., Wang, X., He, B., Mei, C., He, J., Lin, Y., Cao, Q., Li, D., and Shan, H. (2021). Near-infrared fluorescence-guided resection of micrometastases derived from esophageal squamous cell carcinoma using a c-Met-targeted probe in a preclinical xenograft model. J. Contr. Release *332*, 171–183. https://doi.org/10.1016/j.jconrel.2021.02.019.
14. Wu, J., Liu, J., Lin, B., Lv, R., Yuan, Y., and Tao, X. (2021). Met-Targeted Dual-Modal MRI/NIR II Imaging for Specific Recognition of Head and Neck Squamous Cell Carcinoma. ACS Biomater. Sci. Eng. *7*, 1640–1650. https://doi.org/10.1021/acsbiomaterials.0c01807.
15. Wang, J., Li, S., Wang, K., Zhu, L., Yang, L., Zhu, Y., Zhang, Z., Hu, L., Yuan, Y., Fan, Q., et al. (2023). A c-MET-Targeted Topical Fluorescent Probe cMBP-ICG Improves Oral Squamous Cell Carcinoma Detection in Humans. Ann. Surg Oncol. *30*, 641–651. https://doi.org/10.1245/s10434-022-12532-x.
16. Wu, Y., Fan, Q., Zeng, F., Zhu, J., Chen, J., Fan, D., Li, X., Duan, W., Guo, Q., Cao, Z., et al. (2018). Peptide-Functionalized Nanoinhibitor Restrains Brain Tumor Growth by Abrogating Mesenchymal-Epithelial Transition Factor (MET) Signaling. Nano Lett. *18*, 5488–5498. https://doi.org/10.1021/acs.nanolett.8b01879.
17. van Keulen, S., van den Berg, N.S., Nishio, N., Birkeland, A., Zhou, Q., Lu, G., Wang, H.-W., Middendorf, L., Forouzanfar, T., Martin, B.A., et al. (2019). Rapid, non-invasive fluorescence margin assessment: Optical specimen mapping in oral squamous cell carcinoma. Oral Oncol. *88*, 58–65. https://doi.org/10.1016/j.oraloncology.2018.11.012.
18. van Keulen, S., Nishio, N., Fakurnejad, S., van den Berg, N.S., Lu, G., Birkeland, A., Martin, B.A., Forouzanfar, T., Colevas, A.D., and Rosenthal, E.L. (2019). Intraoperative tumor assessment using real-time molecular imaging in head and neck cancer patients. J. Am. Coll. Surg. *229*, 560–567.e1. https://doi.org/10.1016/j.jamcollsurg.2019.09.007.
19. Chen, Y., Wang, S., and Zhang, F. (2023). Near-infrared luminescence high-contrast in vivo biomedical imaging. Nat. Rev. Bioeng. *1*, 60–78. https://doi.org/10.1038/s44222-022-00002-8.
20. Vogel, P., Rückert, M.A., Friedrich, B., Tietze, R., Lyer, S., Kampf, T., Hennig, T., Dölken, L., Alexiou, C., and Behr, V.C. (2022). Critical Offset Magnetic PArticle SpectroScopy for rapid and highly sensitive medical point-of-care diagnostics. Nat. Commun. *13*, 7230. https://doi.org/10.1038/s41467-022-34941-y.
21. Essat, M., Cooper, K., Bessey, A., Clowes, M., Chilcott, J.B., and Hunter, K.D. (2022). Diagnostic accuracy of conventional oral examination for detecting oral cavity cancer and potentially malignant disorders in patients with clinically evident oral lesions: Systematic review and meta-analysis. Head Neck *44*, 998–1013. https://doi.org/10.1002/hed.26992.
22. Mehanna, H.M., Rattay, T., Smith, J., and McConkey, C.C. (2009). Treatment and follow-up of oral dysplasia - a systematic review and meta-analysis. Head Neck *31*, 1600–1609. https://doi.org/10.1002/hed.21131.
23. Nevanpää, T.T., Terävä, A.E., Laine, H.K., and Rautava, J. (2022). Malignant transformation of oral epithelial dysplasia in Southwest Finland. Sci. Rep. *12*, 8261. https://doi.org/10.1038/s41598-022-12441-9.
24. Edwards, P.C. (2014). The natural history of oral epithelial dysplasia: perspective on Dost et al. Oral Surg. Oral Med. Oral Pathol. Oral Radiol. *117*, 263–266. https://doi.org/10.1016/j.oooo.2013.12.399.
25. Speight, P.M., Khurram, S.A., and Kujan, O. (2018). Oral potentially malignant disorders: risk of progression to malignancy. Oral Surg. Oral Med. Oral Pathol. Oral Radiol. *125*, 612–627. https://doi.org/10.1016/j.oooo.2017.12.011.
26. Li, C.H., Haider, S., Shiah, Y.-J., Thai, K., and Boutros, P.C. (2018). Sex Differences in Cancer Driver Genes and Biomarkers. Cancer Res. *78*, 5527–5537. https://doi.org/10.1158/0008-5472.Can-18-0362.
27. Connelly, S.T., and Schmidt, B.L. (2004). Evaluation of pain in patients with oral squamous cell carcinoma. J. Pain *5*, 505–510. https://doi.org/10.1016/j.jpain.2004.09.002.
28. Bhattacharya, A., Janal, M.N., Veeramachaneni, R., Dolgalev, I., Dubeykovskaya, Z., Tu, N.H., Kim, H., Zhang, S., Wu, A.K., Hagiwara, M., et al. (2020). Oncogenes overexpressed in metastatic oral cancers from patients with pain: potential pain mediators released in exosomes. Sci. Rep. *10*, 14724. https://doi.org/10.1038/s41598-020-71298-y.
29. Klasen, C., Wuerdemann, N., Rothbart, P., Prinz, J., Eckel, H.N.C., Suchan, M., Kopp, C., Johannsen, J., Ziogas, M., Charpentier, A., et al. (2023). Sex-specific aspects in patients with oropharyngeal squamous cell carcinoma: a bicentric cohort study. BMC Cancer *23*, 1054. https://doi.org/10.1186/s12885-023-11526-6.
30. Yang, E.C., Tan, M.T., Schwarz, R.A., Richards-Kortum, R.R., Gillenwater, A.M., and Vigneswaran, N. (2018). Noninvasive diagnostic adjuncts for the evaluation of potentially premalignant oral epithelial lesions: current limitations and future directions. Oral Surg. Oral Med. Oral Pathol. Oral Radiol. *125*, 670–681. https://doi.org/10.1016/j.oooo.2018.02.020.
31. Abati, S., Bramati, C., Bondi, S., Lissoni, A., and Trimarchi, M. (2020). Oral Cancer and Precancer: A Narrative Review on the Relevance of Early Diagnosis. Int. J. Environ. Res. Publ. Health *17*, 9160. https://doi.org/10.3390/ijerph17249160.
32. Villa, A., Villa, C., and Abati, S. (2011). Oral cancer and oral erythroplakia: an update and implication for clinicians. Aust. Dent. J. *56*, 253–256. https://doi.org/10.1111/j.1834-7819.2011.01337.x.

33. Carrard, V.C., and van der Waal, I. (2018). A clinical diagnosis of oral leukoplakia; A guide for dentists. Med. Oral Patol. Oral Cir. Bucal *23*, e59–e64. https://doi.org/10.4317/medoral.22292.

34. Meng, X., Zhao, Y., Han, B., Zha, C., Zhang, Y., Li, Z., Wu, P., Qi, T., Jiang, C., Liu, Y., and Cai, J. (2020). Dual functionalized brain-targeting nanoinhibitors restrain temozolomide-resistant glioma via attenuating EGFR and MET signaling pathways. Nat. Commun. *11*, 594. https://doi.org/10.1038/s41467-019-14036-x.

35. Kim, E.-M., Park, E.-H., Cheong, S.-J., Lee, C.-M., Kim, D.W., Jeong, H.-J., Lim, S.T., Sohn, M.-H., Kim, K., and Chung, J. (2009). Characterization, biodistribution and small-animal SPECT of I-125-labeled c-Met binding peptide in mice bearing c-Met receptor tyrosine kinase-positive tumor xenografts. Nucl. Med. Biol. *36*, 371–378. https://doi.org/10.1016/j.nucmedbio.2009.01.005.

36. Wang, H., Li, X., Tse, B.W.-C., Yang, H., Thorling, C.A., Liu, Y., Touraud, M., Chouane, J.B., Liu, X., Roberts, M.S., and Liang, X. (2018). Indocyanine green-incorporating nanoparticles for cancer theranostics. Theranostics *8*, 1227–1242. https://doi.org/10.7150/thno.22872.

37. Naik, K., Janal, M.N., Chen, J., Bandary, D., Brar, B., Zhang, S., Dolan, J.C., Schmidt, B.L., Albertson, D.G., and Bhattacharya, A. (2021). The Histopathology of Oral Cancer Pain in a Mouse Model and a Human Cohort. J. Dent. Res. *100*, 194–200. https://doi.org/10.1177/0022034520961020.

38. Wallace, M.B., Sharma, P., Bhandari, P., East, J., Antonelli, G., Lorenzetti, R., Vieth, M., Speranza, I., Spadaccini, M., Desai, M., et al. (2022). Impact of Artificial Intelligence on Miss Rate of Colorectal Neoplasia. Gastroenterology *163*, 295–304.e5. https://doi.org/10.1053/j.gastro.2022.03.007.

39. Chen, J., Jiang, Y., Chang, T.-S., Joshi, B., Zhou, J., Rubenstein, J.H., Wamsteker, E.J., Kwon, R.S., Appelman, H., Beer, D.G., et al. (2021). Multiplexed endoscopic imaging of Barrett's neoplasia using targeted fluorescent heptapeptides in a phase 1 proof-of-concept study. Gut *70*, 1010–1013. https://doi.org/10.1136/gutjnl-2020-322945.

STAR★METHODS

KEY RESOURCES TABLE

REAGENT or RESOURCE	SOURCE	IDENTIFIER
Antibodies		
anti-MET rabbit monoclonal antibody	Abcam	Cat#ab51067; RRID:AB_880695
Alexa Fluor® 488 Conjugate	Cell Signaling Technology	Cat#4412; RRID:AB_1904025
GAPDH monoclonal antibody	Cell Signaling Technology	Cat#5174; RRID:AB_10622025
HRP conjugated secondary antibodies	Cell Signaling Technology	Cat#98164; RRID:AB_2936818
rabbit IgG isotype antibody	Invitrogen	Cat#02-6102; RRID:AB_2532938
Rabbit monoclonal to MET	Abcam	Cat#ab216574
Alexa Fluor 488 secondary goat anti-rabbit antibody	Cell Signaling Technology	Cat#4412; RRID:AB_1904025
Critical commercial assays		
4-Nitroquinoline N-oxide (4-NQO)	Millipore Sigma	CAS#56-57-5
Experimental models: Cell lines		
FaDu	Shanghai Institute of Biochemistry and Cell Biology	N/A
Cal27	Shanghai Institute of Biochemistry and Cell Biology	N/A
WSU-HN30	Yukacell	N/A
HSF	Yukacell	N/A
Software and algorithms		
ImageJ	Schneider et al.[7]	https://imagej.nih.gov/ij/
NDP.view2	Hamamatsu Photonics, K. K.	https://www.hamamatsu.com/eu/en.html
flowjo	Becton, Dickinson & Company	https://www.flowjo.com/
DPM-III-01	Zhuhai Dipu Medical Technology Co.	https://www.digipmc.com/En
GraphPad Prism	GRAPHPAD SOFTWARE, LLC	https://www.graphpad.com/

EXPERIMENTAL MODEL AND STUDY PARTICIPANT DETAILS

Animal models

Mice were purchased from the experimental animal center of Shanghai Ninth People's Hospital, Shanghai JiaoTong University. The animals were housed in a specific-pathogen-free facility under a 12-h light/12-h dark cycle. The temperature ranged from 24°C to 26°C, and the humidity ranged from 50% to 70%. Male mice were selected for this study to reflect the higher incidence of oral squamous cell carcinoma (OSCC) observed in males in epidemiological studies.[29] The animal experiments were conducted at Shanghai Ninth People's Hospital and approved by the hospital's Ethics Office (approval number SH9H-2020-A620-1), and all procedures were carried out in accordance with NIH standards for laboratory animal care and use. To develop a mimic of subcutaneous human HNSCC tumors, 2×10^6 Cal27 cells in 100 μL of PBS were inoculated into the lower back of 4-week-old BALB/c-nu/nu mice. We conducted the experiments when tumors attained a volume of 100 mm^3–150 mm^3. For the orthotopic HNSCC model, 1.2×10^6 Cal27 cells in 20 μL of PBS were directly inoculated into the tongue of 4-week-old BALB/c-nu/nu mice. Mice were observed daily for tumor growth and weight loss. Images of the tumors were acquired every 2 to 3 weeks. To evaluate the feasibility of NIRFI with surface application of cMBP-ICG for detecting precancerous lesions and early OSCC, we used the 4-NQO-induced OSCC mouse model, which effectively mimics human oral carcinogenesis, dynamically progressing from normal mucosa to hyperplasia, dysplasia, and carcinoma. 4-NQO was dissolved in 2% mother liquor containing 1,2 propylene glycol and diluted to a concentration of 50 μg/mL with sterilized tap water. The solution was stored in a light-protected container and used as drinking water for model animals. Thirty 8-week-old male C57BL/6 mice were randomly assigned to the test group (N = 15) or the control group (N = 15). Mice in the test group received water containing 4-NQO for the initial 12 weeks and then received sterilized tap water. Mice in the control group received a solution of 10 g/mL ethylene glycol in water for the initial 12 weeks and then received sterilized tap water.

Cell lines and cell culture

The HNSCC cell lines FaDu (hypopharyngeal SCC; male, Shanghai Institute of Biochemistry and Cell Biology, Shanghai, China), Cal27 (tongue SCC; male, Shanghai Institute of Biochemistry and Cell Biology), WSU-HN30 (pharynx SCC; male, Yukacell, Shanghai, China) were grown in monolayers at 37°C with 5% CO2. The HSF cell line (keratin epithelial cell; Yukacell) was also used, though its gender is not specified in the available literature, and this limitation is acknowledged. All cell lines were authenticated using short tandem repeat (STR) profiling to confirm their identity. Mycoplasma contamination was tested using PCR-based mycoplasma detection assays, and all cell lines were confirmed to be mycoplasma-free before use. We inoculated the FaDu cells in MEM enriched with 10% (v/v) FBS and 1% PenStrep and the Cal27, WSU-HN30, and HSF cells in DMEM enriched with 10% (v/v) FBS and 1% PenStrep.

Human participants

To better understand the role of MET as a clinical signature for OSCC, we compared the expression patterns of MET between human oral cancer tissues and adjacent nonmalignant tissues in 9 tissue specimens (detailed information in Table S7) from surgical excisions performed at the Department of Pathology of Shanghai Ninth People's Hospital. The mean age of patients in this cohort was 57 years (range: 37–70 years), and the group consisted of 5 females and 4 males, all of East Asian descent. The specimens were from lesions histopathologically classified as premalignant lesion (3 specimens), low-grade cancer (3 specimens), and high-grade cancer (3 specimens). Premalignant lesions were defined as high-grade epithelial neoplasia and SCC *in situ*. Low-grade cancer was defined as lesions in which most of the tumor cells had a nonmalignant appearance and the cancer was well differentiated. High-grade cancer was defined as lesions in which the tumor cells had a very different appearance from that of nonmalignant tissue and were poorly differentiated.[30] All tissue samples were formalin-fixed and paraffin-embedded (FFPE) for histopathological evaluation and immunohistochemistry. Using receiver operating characteristic curve analysis, we evaluated MET's ability to discriminate between tumor and normal tissue. The use of human tissues was approved by the Institutional Review Board at Shanghai Ninth People's Hospital, and all the subjects granted informed consent (approval number SH9H-2020-T147-3). The clinical trial was conducted at Shanghai Ninth People's Hospital and was approved by the institutional review board of the Chinese Clinical Trial Registry (ChiCTR2300074454). Written informed consent was obtained from all patients. The clinical trial protocol is available in the supplemental information. Briefly, from June 2023 through December 2023, fifty patients (aged $\geq$ 18 years) diagnosed with OPMD[25,31–33] were recruited (detailed information is in Table S8). The mean age of participants was 54 years (range: 25–76 years), with a female-to-male ratio of 2:1 (34 females, 16 males). All participants were of East Asian descent. All patients were randomly assigned to two groups (25 *per*group) using a computer-generated random number sequence to minimize selection bias.

METHOD DETAILS

Synthesis and characterization of cMBP-ICG

cMBP peptide was chosen as the targeting ligand on the basis of our previous work[15,16] showing that cMBP has strong docking affinity to MET (KD = 3.96 × 10^{-7} M) and because cMBP has been shown to have potential use in tumor treatment[34] and imaging.[15,35] ICG was selected as the imaging probe because of its high signal-to-background ratio and biological safety.[36]

cMBP-ICG was synthesized by coupling sulfo-ICG-maleimide (Lumiprobe, Hunt Valley, MD, USA) with a custom MET-binding peptide (KSLSRHDHIHHHK).[15] The reaction was conducted in the dark at room temperature and monitored by reverse-phase high-performance liquid chromatography (RP-HPLC). Free ICG dye was removed using RP-HPLC, and the purified cMBP-ICG was lyophilized by China Peptides Co. (Suzhou, China). For imaging studies, 5 μL of PBS was added to 70 ng of lyophilized cMBP-ICG. Detailed synthesis and purification steps are provided in the supplemental information.

In vivo toxicological evaluation of cMBP-ICG

For the toxicological evaluation of cMBP-ICG, we used five 8-week-old male C57BL/6 mice. A 2.5-mM cMBP-ICG solution was administered in place of drinking water for 24 h, after which normal drinking water was restarted. Blood samples were collected from the orbital venous plexus at baseline, 24 h after the start of cMBP-ICG administration, and 14 days after the start of cMBP-ICG administration, and a complete blood cell count (white blood cells, red blood cells, hemoglobin, hematocrit, mean corpuscular volume, mean corpuscular hemoglobin, mean corpuscular hemoglobin concentration, platelets) and blood biochemistry studies (alanine aminotransferase, aspartate aminotransferase, alkaline phosphatase, blood urea nitrogen, creatine, glucose, total protein, albumin) were performed.

Confocal and light microscopy imaging

Immunohistochemistry (IHC) and immunofluorescence (IF) were performed at the Shanghai Institute of Materia Medica (Chinese Academy of Sciences, China) with a confocal microscope (NOL-LSM 710, Carl Zeiss, Germany).

For IHC, paraffin-embedded, formalin-fixed 3-μm sections were deparaffinized with EZPrep buffer (Ventana Medical Systems, Tucson, AZ, USA); antigen retrieval was performed with CC1 buffer (Ventana Medical Systems); and sections were blocked for 30 min with Background Buster solution (Innovex, Richmond, CA). Sections were incubated with an anti-MET rabbit monoclonal antibody (ab51067; Abcam, Shanghai, China) that specifically binds both human and mouse MET for 5 h at a 1:300 dilution. For protein

detection, a DAB detection kit (DAB-0031; MXB Biotechnologies, China) was used according to the manufacturer's instructions, and sections were counterstained with hematoxylin and coverslipped with Permount (Fisher Scientific, Pittsburgh, PA).

For IF, detection was also performed with the anti-MET rabbit monoclonal antibody (ab51067), followed by incubation with Alexa Fluor 488 secondary goat anti-rabbit antibody (#4412, Cell Signaling Technology, MA, USA) prepared according to the manufacturer's instructions. Sections were counterstained with 4′,6-diamidino-2-phenylindole (DAPI) for 10 min and coverslipped with Mowiol mounting medium (Sigma-Aldrich, St. Louis, MO). Incubating with the rabbit IgG instead of the primary antibody controlled for nonspecific binding of the secondary antibody.

Hematoxylin-eosin (H&E) staining of neighboring sections was done to assess the morphological properties of the tissues. Digitalization of the tumor sections was done with a NanoZoomer Digital Pathology scanner (NanoZoomer 2.0-RS, Hamamatsu Photonics) for quantification of the MET proteins. NanoZoomer Digital Pathology software (NDP.view2, version 2.9.29) was employed to assess at least 10 fields per section. In the IHC-stained tissues, we performed thresholding on the brown (MET) and blue (tissue) sites, and we computed the relative MET-positive area by dividing the brown area by the overall tissue area. The MET-positive area was computed via thresholding the red fluorescent area and dividing it by the overall tissue area, which was assessed on the basis of the intensity of blue fluorescence in all nuclei that were thresholded via DAPI staining. The determined intensities of fluorescence were averaged over all nuclei in every field of view, with intensity values between 0 and 255. Correlation of cMBP uptake and MET expression was determined by the inter- and intra-cellular co-localization of the targeted fluorescent probe with MET antigen in cell climbing slides or histological sections.

Western blotting

For western blotting analysis of MET protein expression, RIPA lysis buffer (Beyotime Biotechnology, Shanghai, China) was used to concentrate proteins from cell lines. Electrophoresis was performed with sodium dodecyl sulfate polyacrylamide gels (Beyotime Biotechnology) using 10 μg of purified protein in each cell line or human esophageal tissue. The separated proteins were transferred to microporous polyvinylidene difluoride membranes (Roche, USA) and then blocked using 5% bovine serum albumin (Scientific Phygene, Fuzhou, China). The membranes were then incubated in anti-MET rabbit monoclonal antibody (ab51067) or GAPDH monoclonal antibody (#5174, Cell Signaling Technology) at 4°C overnight. After washing and incubation with HRP-conjugated secondary antibodies (#98164, Cell Signaling Technology) at room temperature for 1 h, Gension Enhanced ECL (solution A: solution B = 1:1) (Gension, Guangzhou, China) was used to detect protein bands, and they were imaged on a ChemiDocXRS + imaging system (Bio-Rad, USA). Semiquantitative assessment of MET along with GAPDH was done with ImageJ software (National Institutes of Health, USA).

Flow cytometry

For flow cytometry analysis of MET expression, adherently grown cells were detached using pancreatic enzyme (Sigma-Aldrich, St. Louis, MO, USA), and harvested cells were incubated with 300 μL of rabbit IgG isotype antibody (02–6102; Invitrogen) or rabbit monoclonal antibody to MET (ab216574) at 4°C for 30 min. Subsequently, cells were rinsed in PBS and incubated with Alexa Fluor 488 secondary goat anti-rabbit antibody (#4412) for 30 min. After rinsing, cells were resuspended in 400 μL of PBS. Fluorescence analysis was performed using a flow cytometer (CytoFLEX LX, Beckman Coulter, Inc., IN, USA) with a count of 1×10^4 living cells per sample. The flow cytometry data were analyzed with FlowJo software (FlowJo, version 10.9.0, Ashland, OR, USA).

NIRFI with cMBP-ICG to identify OSCC in CDXs

To test NIRFI with cMBP-ICG in mice with CDXs, we injected a solution of 5 μL of PBS and 70 ng of cMBP-ICG lyophilized powder into the mouse tongues and then performed fluorescence imaging. The mice were maintained under anesthesia with ketamine (0.1 mg/g body weight) during probe injection and imaging. A preclinical fluorescence laryngoscope imaging platform (DPM-III-01, Zhuhai Dipu Medical Technology Co., Ltd.) was used for real-time fluorescence imaging. Photos were acquired before and 30 min after injection of the probe. We used the same instrument settings in all the procedures involving imaging (exposure time of 30 ms, excitation power of 20%, gain of 3 dB). In addition, we maintained the distance between the laryngoscope and the tissue surface at approximately 10 mm. To acquire the photos, we slowly scanned the tumor area along with neighboring nonmalignant mucosa. In the course of this process, we utilized real-time white light imaging for visual guidance, as well as focusing. ImageJ software was used for image analysis. The tumor-to-background ratio (TBR) was defined as the fluorescence intensity of the tumor divided by the fluorescence intensity of the adjacent tissue. We harvested the whole tongues for *ex vivo* imaging. Following biodistribution assessment, we fixed the tumor tissues in 4% PFA along with optimal cutting temperature compound (SAKURA, USA) for IHC assessment accompanied by frozen-tissue immunofluorescence imaging.

Tumors and MET expression in the 4-NQO model

Three mice from each group—4-NQO-treated and control—were sacrificed at 0, 12, 16, 20, and 24 weeks, respectively. Tissue samples from the tongues of sacrificed mice were collected and subjected to histopathological analysis to determine tumor development time and stage and MET expression (Figure S5). The mice were monitored at 12, 16, 20, and 24 weeks using 9.4T magnetic resonance imaging (Biospec94/30USR, Bruck, Germany). In the imaging protocols, the parameters were set as follows: For the T1-RARE sequence, the echo time was 6.00 ms, and the repetition time was 800.00 ms. The flip angle was 180.00°. The pixel spacing was

0.075 mm × 0.075 mm, and the slice thickness was 0.50 cm. For the T2-TurboRARE sequence, the echo time was 33.35 ms, and the repetition time was 2,500.00 ms. The flip angle remained at 180.00°, with the same pixel spacing and slice thickness as for the T1-RARE sequence.

NIRFI to identify OPMD in the 4-NQO model

To test NIRFI with cMBP-ICG in the 4-NQO-induced OSCC model, we used forty 8-week-old male C57BL/6 mice A solution of 5 μL of PBS and 70 ng of cMBP-ICG lyophilized powder was prepared. Forceps were used to expose the tongue, and the cMBP-ICG solution was dripped onto the tongue for 1 min, ensuring complete exposure of the entire oral mucosa. After the mouse tongue was washed twice with PBS to eliminate any residual unbound compounds, the preclinical NIRFI platform described above under "NIRFI with cMBP-ICG to identify OSCC in CDXs" was utilized for real-time NIRFI. Photos were obtained using the same protocol as described.[15] TBR was defined as the fluorescence intensity of the tumor divided by the fluorescence intensity of the adjacent tissue. During topical application of the cMBP-ICG solution and subsequent imaging, mice were maintained under anesthesia with ketamine at a dose of 0.1 mg per gram of body weight.

Twenty to 24 weeks after the start of 4-NQO induction, the abundance and distribution of tongue lesions in mice closely resembled those observed in human OPMDs.[37] Consequently, real-time NIRFI-assisted biopsies were performed at 20 weeks and 24 weeks. The 40 mice were stratified on the basis of time since initiation of 4-NQO induction (20 weeks or 24 weeks) and were randomly allocated into two groups (1:1) using a tandem design as described previously.[38] Mice in each group underwent two biopsies. In the NIRFI-assisted biopsy group, NIRFI-assisted biopsy was the first biopsy, and COE-based biopsy was the second biopsy. In the COE-based biopsy group, COE-based biopsy was the first biopsy, and NIRFI-assisted biopsy was the second biopsy.[39] The criterion standard was findings on histopathological evaluation of H&E-stained, paraffin-embedded tissue sections. All biopsied lesions were graded by pathologists specializing in oral lesions who were blinded to group assignments. Lesions were classified as normal epithelial tissue, low-grade dysplasia (LGD), high-grade dysplasia (HGD), carcinoma *in situ* (CIS), or invasive carcinoma (ICA). All lesions within the remaining tongue tissues were meticulously annotated on slides by a pathologist with 20 years of expertise in oral and maxillofacial pathology. The numbers and pathological classifications of the biopsied lesions and the lesions within the remaining tongue tissues were documented for subsequent analysis.

Exploratory clinical trial

A single-center prospective randomized controlled trial of NIRFI-assisted biopsy versus COE-based biopsy was approved by the institutional review board of the Chinese Clinical Trial Registry (ChiCTR2300074454). The inclusion and exclusion criteria are detailed in Figure S6. Eligible patients were randomized 1:1 to the real-time NIRFI-assisted biopsy group or COE-based biopsy group using a computer-generated random sequence.

The oral conditions of all patients were thoroughly assessed by an experienced oral mucosal specialist, who selected and documented what the specialist judged to be the most appropriate biopsy site and assigned a clinical diagnosis of LGD, HGD, or OSCC. Following this, all patients underwent NIRFI, during which the NIRFI operator selected and documented what the operator judged to be the most appropriate biopsy site and assigned a clinical diagnosis of LGD, HGD, or OSCC.[15] Subsequently, patients in the NIRFI-assisted biopsy group underwent biopsy at the site selected by the NIRFI operator, while subjects in the COE-based biopsy group underwent biopsy at the site selected by the oral mucosal specialist without reference to NIRFI. The NIRFI procedure was detailed in our previous report.[15] All patients were assessed by the same experienced oral mucosal specialist. After the NIRFI procedure, mucosal toxicity and patients' subjective experiences were recorded. Six months after biopsy, all patients were re-examined visually to check for new lesions, and any newly identified lesions were biopsied using the biopsy method used previously. All biopsy specimens were sectioned, embedded in paraffin, stained with H&E, subjected to histopathological analysis, and categorized as negative (normal epithelium, LGD) or positive (HGD, SCC). Patients, pathologists, and data analysts were blinded to the intervention.

QUANTIFICATION AND STATISTICAL ANALYSIS

For real-time NIRFI-assisted biopsy in mice, logistic mixed models were employed to analyze the detection rate and missed detection rate, considering treatment group (NIRFI-assisted biopsy vs. COE-based biopsy) and time since initiation of 4-NQO induction (20 weeks vs. 24 weeks). The detection rate was calculated as the number of lesions histologically confirmed as HGD, CIS, or ICA on the first biopsy divided by the total number of samples histologically confirmed as HGD, CIS, or ICA. The missed detection rate was defined as the number of lesions histologically confirmed as HGD, CIS, or ICA on the second biopsy divided by the total number of samples histologically confirmed as HGD, CIS, or ICA. The two-sided 95% confidence interval was computed for the treatment odds ratio (OR) between the test and control groups. An OR less than 1 for missed diagnosis rate indicates that NIRFI-assisted biopsy is superior to COE-based biopsy due to lower miss rates, while an OR greater than 1 for detection rate suggests that NIRFI-assisted biopsy is superior to COE-based biopsy due to higher detection rates. The chi-square test was used to determine the sensitivity of missed diagnosis rates and detection rates, while the Wilcoxon rank-sum test was used to analyze the mean number of neoplasms detected on the second biopsy and the mean number of neoplasms detected on the second biopsy with no lesion detected on the first biopsy.

For the clinical trial, the primary aim was to determine if NIRFI-assisted biopsy had higher accuracy in diagnosing HGD, the presence of which is a key factor in surgical decisions, and identified more malignant lesions than COE-based biopsy. The secondary aim was to develop a model using NIRFI for more accurate future diagnoses. The mean fluorescence intensity and TBR were computed for all lesions and subjected to a stratified analysis based on pathological findings to investigate the utility of these metrics in diagnostic classification. This exploratory clinical study also included a critical assessment of adverse effects of the cMBP-ICG solution, such as anaphylaxis (including mucosal edema), and whether the taste was acceptable. The detailed protocol for assessing the diagnostic performance of NIRFI-assisted biopsy and COE-based biopsy is illustrated in Figure 3 and described in the Clinical Trial Protocol in the supplemental information.

Statistical analyses were performed using GraphPad Prism version 9.5 and Python version 3.12.4 for advanced data processing and visualization. Data are presented as mean values with error bars representing standard deviations of biological replicates. Unpaired two-tailed Student's t-tests were used for two-group comparisons. One-way and two-way analysis of variance (ANOVA) was performed for multiple-group comparisons, followed by Tukey's post hoc test for pairwise comparisons where significant differences were detected. ROC curves were applied to evaluate the diagnostic performance of MET expression and fluorescence-based imaging related key variables, with AUC values used to quantify classification accuracy. Logistic regression analysis was applied to assess factors associated with missed detection rates and detection rates in NIRFI-assisted and COE-based biopsy groups. The results are presented as odds ratios (ORs) with 95% confidence intervals (CIs). A P-value < 0.05 was considered statistically significant. Significance levels are denoted in figures with asterisks ($^{*}p < 0.05$, $^{**}p < 0.01$, $^{***}p < 0.001$, $^{****}p < 0.0001$).

ADDITIONAL RESOURCES

The clinical trial is registered under registration number ChiCTR2300074454. (https://www.chictr.org.cn/showproj.html?proj=200268).